

Structural, elastic and thermal properties of cementite (Fe_3C) calculated using Modified Embedded Atom Method

Laalitha S. I. Liyanage

*Department of Physics and Astronomy, Mississippi State University, Mississippi State, MS 39762, USA and
Center for Advanced Vehicular Systems, Mississippi State University, Mississippi State, MS 39762, USA*

Seong-Gon Kim*

*Department of Physics and Astronomy, Mississippi State University, Mississippi State, MS 39762, USA and
Center for Computational Sciences, Mississippi State University, Mississippi State, MS 39762, USA*

Jeff Houze, Sungho Kim, and M. A. Tschopp

Center for Advanced Vehicular Systems, Mississippi State University, Mississippi State, MS 39762, USA

M. I. Baskes

*Department of Mechanical and Aerospace Engineering,
University of California, San Diego, La Jolla, CA 92093, USA and
Los Alamos National Laboratory Los Alamos, NM 87545, USA*

M. F. Horstemeyer

*Department of Mechanical Engineering, Mississippi State University, Mississippi State, MS 39762, USA and
Center for Advanced Vehicular Systems, Mississippi State University, Mississippi State, MS 39762, USA*

(Dated: April 25, 2012)

Structural, elastic and thermal properties of cementite (Fe_3C) were studied using a Modified Embedded Atom Method (MEAM) potential for iron-carbon (Fe-C) alloys. Previously developed Fe and C single element potentials were used to develop a Fe-C alloy MEAM potential, using a statistically-based optimization scheme to reproduce the heat of formation of Fe-C alloys in L_{12} , B_1 , and cementite structures, as well as the interstitial energies of C in bcc Fe. The stability of cementite was investigated by molecular dynamics simulations at high temperatures. The nine single crystal elastic constants for cementite were obtained by computing total energies for strained cells. Polycrystalline elastic moduli for cementite were calculated from the single crystal elastic constants of cementite. The formation energies of (001), (010), and (100) surfaces of cementite were also calculated. The melting temperature and the variation of specific heat and volume with respect to temperature were investigated by performing a two-phase (solid/liquid) molecular dynamics simulation of cementite. The predictions of the potential are in good agreement with first-principles calculations and experiments.

PACS numbers: 61.50.Lt, 62.20.de, 61.72.jj, 68.35.Md, 71.15.Pd

I. INTRODUCTION

Steel alloys are the most widely used structural materials due to their abundance, all-purpose applicability and low cost. The main carbide in steel alloys is cementite, which forms as a precipitate. Cementite has a direct impact on the mechanical, structural, and thermal properties of steel. Therefore, the ability to describe and predict properties of cementite at the nanoscale is essential in the study and design of new steels. Atomistic simulation methods, such as molecular dynamics or Monte Carlo simulations, offer an efficient and reliable route to investigating nanoscale mechanics pertaining to cementite in steel alloys. Each of these methods requires accurate interatomic potentials to find the energy of the system under investigation. However, first-principles calculations—albeit the most reliable—are incapable of simulating the number of atoms required for realistic calculations due to unreasonable memory and processing-time requirements.

Therefore, semi-empirical potential methods are being explored as a suitable alternative.

Among the spectrum of semi-empirical formulations, the Modified Embedded Atom Method (MEAM), originally proposed by Baskes et al.¹, has been shown to accurately predict properties of most crystal structures, such as bcc, fcc, hcp, and even diatomic gases, in good agreement with experiments or first-principles calculations. MEAM is extended from the Embedded Atom Method (EAM)² to include the directionality of bonds. In the original MEAM formalism, only the first-nearest neighbor (1NN) interactions were considered.¹ Lee and Baskes³ later extended the original formalism to include the screened second-nearest neighbor (2NN) interactions. Further details of the MEAM formalism can be found in Ref. 1 and 3.

One of the commonly used 2NN MEAM potential for the Fe-C system developed by Byeong-Joo Lee⁴ is designed to predict the interactions of interstitial C atoms with defects such as vacancies. According to Fang et

al.,⁵ Lee's potential predicts a negative heat of formation for cementite. Lee's potential also predicts that cementite is only stable up to a temperature of 750 K.⁵ Experimentally, however, cementite is metastable with a positive heat of formation.⁶ Moreover, according to the Fe-C phase diagram,⁷ cementite is stable up to 1420 K. Among recent interatomic potentials^{8–12} for the Fe-C system, EAM potentials by Lau et al.⁹ and Ruda et al.¹¹ and the analytical bond order potential (ABOP) by Henriksson et al.¹² all promise to predict properties of cementite reasonably well. In the potentials by Lau et al.⁹ and Ruda et al.,¹¹ however, the single element potential for C does not predict properties of both graphite and diamond well. This is due to the limited ability of EAM to describe the bare C-C interaction successfully.¹³ We note that a successful interatomic potential for an alloy system should not only predict the properties of the alloy correctly, but it should also predict the properties of the individual alloying elements in their natural crystal structures accurately. The ABOP by Henriksson et al.¹² predicts properties of cementite as well as Fe and C accurately; however, ABOPs are not applicable to simulations involving interfaces and surfaces.¹⁴ Also ABOPs are restricted to considering only 1NN interactions.^{14,15} Some of the more recent potentials for the Fe-C system are implemented using in-house developed molecular dynamics codes, which limits the potentials' transferability.

In the present work, we develop a 2NN MEAM potential for the Fe-C alloy system that accurately predicts the structure and properties of cementite. Our Fe-C alloy potential is based on previously developed 2NN MEAM potentials for Fe¹⁶ and C¹⁷ in their pure forms. The C MEAM potential predicts both diamond and graphite as minimum energy structures with almost degenerate energies. Using the Fe and C single element potentials, the alloy potential for Fe-C was constructed by fitting to the heat of formation of Fe-C alloys in the B₁ and L₁₂ structures, and cementite, as well as the interstitial energies of C in bcc Fe.

II. METHODS

For all atomistic simulations described in this paper, we have used MEAM as implemented in LAMMPS,^{18,19} the classical molecular dynamics simulation code from Sandia National Laboratories. Some of the reference data required for potential construction and validation are not readily available from experiments. In these cases, we performed the first-principles calculations using Density Functional Theory (DFT)^{20,21} and Projector Augmented Wave (PAW) pseudopotentials.²² Electron exchange and correlation were treated with Generalized Gradient Approximation (GGA) as parameterized by Perdew et al.²³ Brillouin zone sampling was performed using the Monkhorst-Pack scheme,²⁴ with a Fermi-level smearing of 0.2 eV applied using the Methfessel-Paxton method.²⁵ Geometric optimizations were carried out us-

ing the conjugate gradient minimization method.²⁰ The constructed Fe-C alloy potential was optimized through a statistically-based optimization scheme to reproduce heat of formation of Fe-C alloys in the B₁ and L₁₂ structures, and cementite, as well as the interstitial energies of C in bcc Fe.

The MEAM potential was constructed by adjusting the potential parameters to reproduce several selected target values using a statistically-based optimization scheme developed by Tschopp et al.²⁶ This scheme uses Latin Hypercube Sampling (LHS),²⁷—a stratified random sampling approach—to sample the N -parameter space, where N is the number of potential parameters sensitive to the target values chosen. A sensitivity analysis was completed at the beginning of the optimization to determine parameters of the potential model most sensitive to the targets. Next, random sampling of the parameter space was done using LHS, with 4000 different potential parameter combinations. Then analytical models were generated to provide a representation of the correlation between potential parameters and target values. Once the models were generated, a multi-objective optimization was executed to determine the best possible values for the parameters.

III. MEAM POTENTIALS

A. Single element potentials

The single element MEAM potential parameters are presented in Table I. The parameters for Fe are from the MEAM potential developed by Lee et al.,¹⁶ and the parameters for C are from Uddin et al.¹⁷

1. Energy vs. volume curves

Energy variation with respect to volume or nearest neighbor distance is considered an important test of validity of interatomic potentials. Here we present the energy *vs.* volume curves generated by the single element potential for Fe and energy *vs.* nearest neighbor distance curves generated by the single element potential for C. Fig. 1 shows the energy *vs.* volume curve for bcc Fe compared to the curves generated by DFT calculations and experimental data. It is well known that DFT overestimates the cohesive energy.²⁸ Therefore, the DFT curve is shifted vertically by a constant amount to the experimental cohesive energy at the equilibrium volume to aid the comparison of the curves. Due to overbinding, the DFT's prediction for the equilibrium volume is underestimated.²⁹ Therefore, the DFT curve sits to the left of the experimental curve. The experimental curve was constructed from Murnaghan's equation of state^{30,31} using the experimental bulk modulus, cohesive energy, and atomic volume listed in Table II. We also tested the stability of Fe in several different crystal structures including bcc, fcc and hcp structures as shown in Fig. 2.

TABLE I. Set of the MEAM potential parameters for pure Fe and C. The parameters include: cohesive energy per atom E_c (eV), equilibrium nearest neighbor distance of the reference structure r_e (Å), cutoff radius r_{cut} (Å), density scaling factor ρ_0 , embedding energy scaling factor A , exponential decay factor for the universal energy α , additional cubic term in the universal energy equation a_3 , atomic density exponential decay factors $\beta^{(0-3)}$, weighting factors for atomic densities $t^{(0-3)}$, and angular screening parameters C_{max} and C_{min} . The bcc and diamond lattices are chosen as the reference structures for Fe and C, respectively.

Element	E_c	r_e	r_{cut}	A	α	a_3	ρ_0	$\beta^{(0)}$	$\beta^{(1)}$	$\beta^{(2)}$	$\beta^{(3)}$	$t^{(0)}$	$t^{(1)}$	$t^{(2)}$	$t^{(3)}$	C_{max}	C_{min}
Fe	4.28	2.469	4.5	0.585	5.027	0.3	1.0	3.8	2.0	0.9	0.0	1.0	-0.8	12.3	2.0	1.9	2.8
C	7.37	1.545	4.5	1.49	4.38	0.0	5.49	4.26	5.0	3.2	3.98	1.0	7.5	1.04	-1.01	0.68	2.0

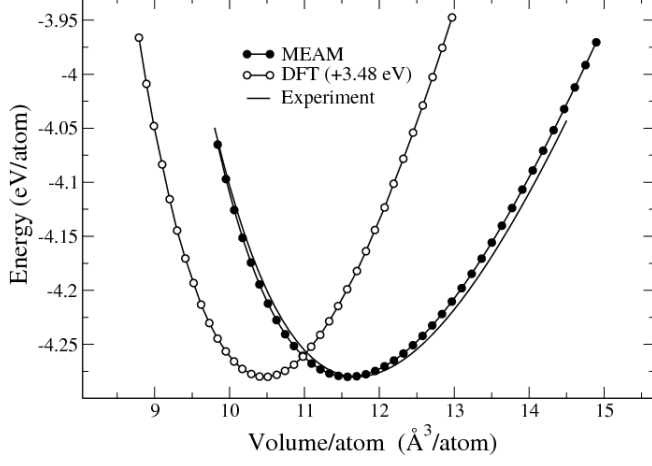


FIG. 1. Comparison of energy *vs.* volume curves for Fe in its most stable bcc structure. The solid curve is constructed from experimental values in Table II. For comparison, the DFT curve is shifted vertically to match the experimental cohesive energy of Fe at the equilibrium volume.

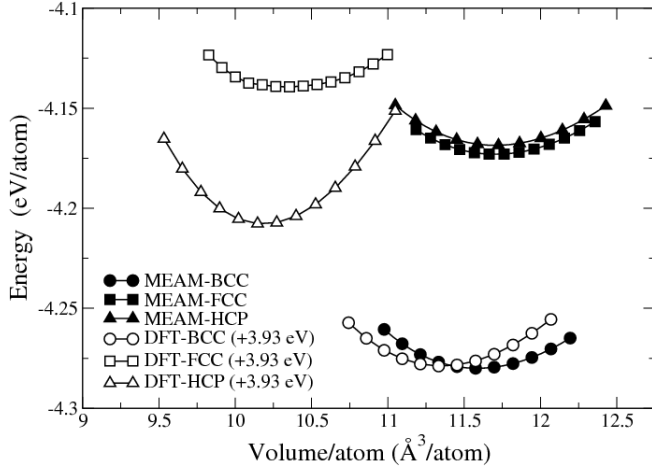


FIG. 2. Comparison of energy *vs.* volume curves for Fe in bcc, fcc and hcp crystal structures. For ease of comparison, the DFT curves are shifted vertically by a constant value equal to the difference between experimental and DFT cohesive energies of Fe in bcc at equilibrium volumes.

The Fe MEAM potential correctly predicts that bcc is the most stable structure, as observed in experiment and

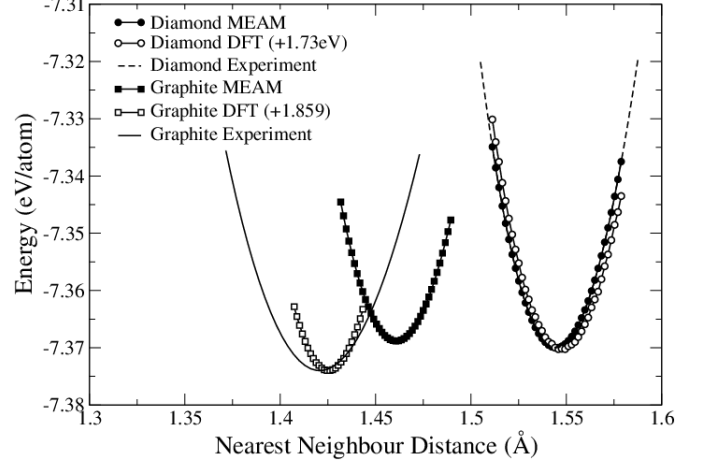


FIG. 3. Comparison of energy *vs.* nearest neighbor distance curves for C in diamond and graphite structures. The solid curve is constructed from experimental values in Table II. For comparison, the DFT curve is shifted vertically to the experimental cohesive energy at the equilibrium nearest neighbor distance.

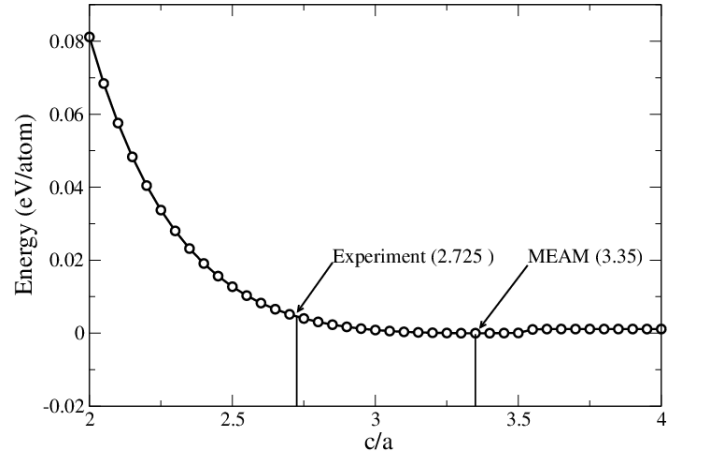


FIG. 4. Cohesive energy of graphite as a function of the c/a ratio. Energy at zero is set to the minimum energy predicted by MEAM.

the first-principles methods. MEAM predicts that fcc and hcp Fe are much closer in energy and have a larger volume than that calculated from DFT.

C single element MEAM potential predicts both diamond and graphite to be stable structures. Energy *vs.* nearest neighbor distance curves for diamond and graphite are shown in Fig. 3. The experimental curves were constructed from the Rose's equation of state³² using the experimental bulk modulus, cohesive energy and nearest neighbor distance, as listed in Table II. MEAM predictions for diamond and graphite are in good agreement with experiment. MEAM predicts almost degenerate cohesive energies for graphite and diamond, while DFT predicts graphite to be ~ 0.1 eV more stable than diamond. For graphite, DFT predicts a first-nearest neighbor (1NN) distance in good agreement with experiment, while MEAM predicts a 1NN distance $\sim 3\%$ greater than the experimental value. MEAM optimized the c/a ratio of the graphite structure to 3.35. This does not agree well with the experimental value of 2.725.³³ This disagreement is due to the incorrect prediction of interlayer interactions of graphite, which are dominated by van Der Waals forces, that are not described by MEAM. However, the dependence of cohesive energy on the c/a ratio is small. As illustrated in Fig. 4, the difference in cohesive energy of graphite between the experimental and MEAM c/a ratio is ~ 4 meV/atom. In constructing the energy *vs.* nearest neighbor distance curves for graphite, the inter-planar distance was scaled with the lattice constant. The experimental ratio was used in the generation of the DFT curve, while the MEAM curve was constructed with the predicted c/a ratio.

2. Single element material properties

The cohesive energy, equilibrium lattice constants and bulk moduli for bcc Fe, graphite, and diamond were determined by fitting Murnaghan's equation of state^{30,31} to the energy *vs.* volume curves generated by MEAM. The single element material properties compared to experimental values are given in Table II.

B. MEAM potential for the Fe-C alloy

The MEAM potential parameters for the Fe-C alloy potential were constructed by fitting the heat of formation of B_1 , L_{12} , and cementite, and to the interstitial energies of C in bcc Fe. Fe_3C in the L_{12} structure and FeC in the B_1 structure are hypothetical crystal structures that do not exist in nature. Therefore, properties of Fe-C in L_{12} and B_1 crystal structures were obtained by first-principles calculations. We also used the first-principles calculations to obtain the interstitial energies of C in the bcc Fe lattice at octahedral and tetrahedral positions. The potential was constructed using a statistically-based optimization scheme developed by Tschopp et al.²⁶ More weight was given to the set of target values that reproduces the correct order of stability of the two C interstitial energies in bcc Fe and the heat of formation of B_1 ,

TABLE II. Material properties predicted by the single element MEAM potentials. E_c is the cohesive energy (eV/atom); a and c are the equilibrium lattice constants (\AA); B is the bulk modulus (GPa); and Ω_0 is the equilibrium atomic volume ($\text{\AA}^3/\text{atom}$). Experimental data are given in parentheses. Experimental values for equilibrium atomic volume were calculated from the experimental lattice parameter(s).

Property	bcc Fe	diamond	graphite
E_c	-4.29 (-4.28 ^a)	-7.37 (-7.37 ^c)	-7.369 (-7.374 ^d)
B	177 (168 ^b)	443 (443 ^c)	176 (286 ^d)
a	2.85 (2.86 ^b)	3.57 (3.567 ^c)	2.53 (2.461 ^d)
c	—	—	8.476 (6.709 ^d)
Ω_0	11.57 (11.70)	5.67 (5.67)	11.74 (8.80)

^a Philipsen et al.²⁸

^b Wang et al.³⁴

^c Ref. 35 and 36 as reported by Fahy et al.³⁷

^d Ref. 30 and 38 as reported by Yin et al.³³

L_{12} , and cementite structures. The final parameters of the alloy potential are presented in Table III.

Table IV lists the MEAM prediction of the target properties used for fitting of the potential compared to DFT and experimental values, and to the interatomic potentials by Ruda et al.¹¹ and Henriksson et al.¹² The orders of stability of B_1 , L_{12} , and cementite structures are predicted correctly compared with DFT results. MEAM predicts the heat of formation of B_1 and L_{12} structures in good agreement with DFT values. MEAM prediction of the heat of formation of cementite is also in good agreement with DFT and experimental data. The MEAM-predicted interstitial energies of C in tetrahedral and octahedral positions of bcc Fe have the same order of magnitude as in DFT predictions. Also like DFT, MEAM predicts the octahedral interstitial to be more stable than the tetrahedral interstitial.

1. Energy *vs.* volume curves for B_1 and L_{12} structures

The cohesive energy of Fe-C in the B_1 and L_{12} crystal structures as a function of the atomic volume is shown in Figs. 5 and 6, respectively. For the B_1 structure, MEAM predicts an atomic volume $\sim 11\%$ less, and a bulk modulus $\sim 0.3\%$ less than the DFT results. The MEAM prediction for the L_{12} structure gives an atomic volume $\sim 11\%$ greater, and a bulk modulus 35% less than DFT. As mentioned earlier, DFT overestimates the cohesive energy. Therefore, to aid the comparison in these figures, the DFT curve is shifted vertically by a constant amount to the MEAM-predicted cohesive energy at the equilibrium nearest neighbor distance.

TABLE III. The MEAM potential parameters for the Fe-C alloy system. The parameters include: heat of formation of the reference structure Δ [eV], equilibrium nearest neighbor distance of the reference structure r_e [Å], cutoff radius r_{cut} [Å], embedding energy scaling factor A , exponential decay factor for the universal energy α , additional cubic term in the universal energy equation a_3 , and angular screening parameters C_{max} and C_{min} . The triplet (a,b,c) represents the configuration with c atom in between a and b atoms. The B_1 lattice is chosen as the reference structure.

Δ	r_e	r_{cut}	α	a_3	C_{max}				C_{min}			
					(Fe,Fe,C)	(Fe,C,C)	(Fe,C,Fe)	(C,C,Fe)	(Fe,Fe,C)	(Fe,C,C)	(Fe,C,Fe)	(C,C,Fe)
0.002	1.92	4.5	4.75	0.125	2.8	2.8	2.8	2.8	0.06	2.0	2.0	0.5

TABLE IV. Materials properties of Fe-C alloys used for the MEAM potential construction. Heat of formation per atom (eV/atom) of Fe-C alloys in B_1 , L_{12} , and cementite structures; the interstitial energies of C in bcc Fe (eV). The predictions from the present work (MEAM) are compared with those from DFT and other interatomic potentials^{11,12}. Experimental data are given in parentheses.

Property	DFT (Expt.)	MEAM	Ruda	Henriksson
ΔH_f (B_1)	0.29	0.17		
ΔH_f (L_{12})	0.36	0.45		
ΔH_f (Cementite)	0.01 (0.05 ^a)	0.06	0.18	0.03
C interstitial (Tetrahedral)	2.14	1.74	2.08	1.50
C interstitial (Octahedral)	1.25	1.55	1.81	1.18

^a Meschel et al.⁶

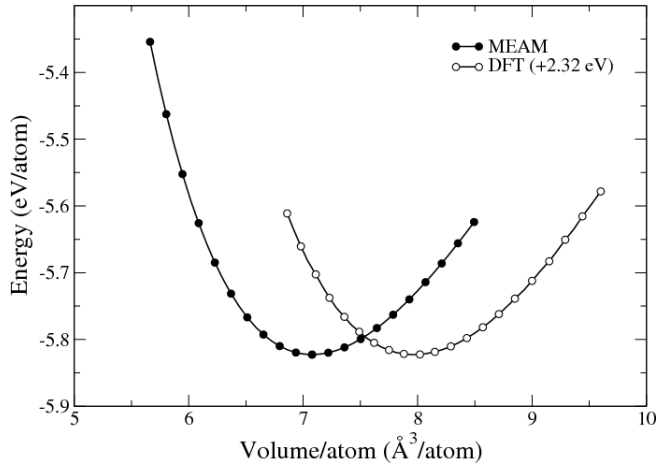


FIG. 5. Comparison of the energy *vs.* volume curves of Fe-C alloy system in the B_1 structure. DFT curve is shifted vertically to the MEAM-predicted cohesive energy at the equilibrium nearest neighbor distance to aid the comparison with the MEAM curve.

2. Elastic constants of FeC in the B_1 crystal structure

Elastic constants of Fe-C in the B_1 crystal structure were calculated using the Fe-C MEAM potential and listed in Table V in comparison with DFT calculations. They were calculated using the deformation matrix presented in Jiang et al.³⁹ In linear elastic theory, deformation energy is a function of strain. Distortion energies (ΔE) calculated for strains (δ) equal to $\pm 2\%$ and $\pm 0.1\%$ were fitted to $\Delta E = k_2\delta^2 + k_3\delta^3$. DFT calculations were performed for $\delta = \pm 2\%$ for comparison.

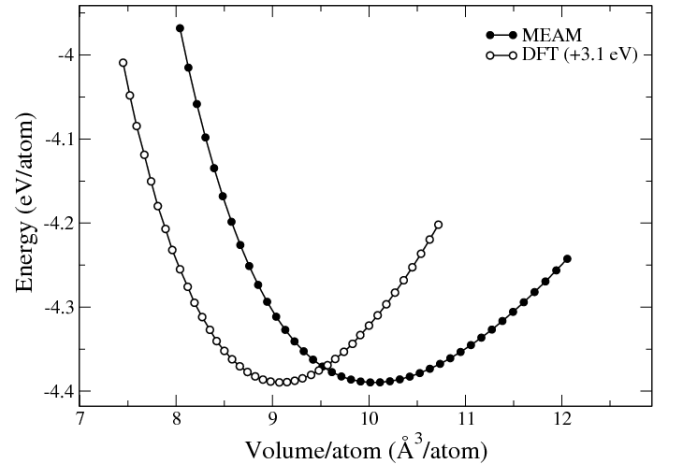


FIG. 6. Comparison of the energy *vs.* volume curves of Fe-C alloy system in the L_{12} structure. DFT curve is shifted vertically to the MEAM-predicted cohesive energy at the equilibrium nearest neighbor distance aid the comparison with the MEAM curve.

The single-crystal elastic constants were obtained using the relationships for the quadratic coefficient k_2 listed in Jiang et al. The present MEAM's result for c_{11} compares reasonably well with the DFT result. c_{12} is predicted at a lower value than DFT, but it is in the same order of magnitude. MEAM prediction of c_{44} is significantly larger than the DFT result.

TABLE V. Elastic moduli (GPa) of FeC in the B₁ structure. The predictions from the present work (MEAM) are compared with those from DFT.

Property	DFT	MEAM	
	$\delta = \pm 2\%$	$\delta = \pm 2\%$	$\delta = \pm 0.1\%$
c_{11}	601	570	566
c_{12}	589	213	213
c_{44}	83	391	389

IV. STRUCTURAL AND ELASTIC PROPERTIES OF CEMENTITE

We tested the present MEAM potential further by computing the structural properties of cementite including the equilibrium lattice parameters, the equilibrium volume per atom, and the heat of formation. These properties are presented in Table VI with comparison to DFT, experiment, and interatomic potentials by Ruda et al.¹¹ and Henriksson et al.¹² As noted in Sec. IIIB, MEAM prediction of the heat of formation of cementite is in excellent agreement with DFT and experimental data. Henriksson's potential also predicts a value in good agreement with DFT and experiment, while Ruda's potential predicts a much larger value. Lattice constants of the present MEAM and literature potentials^{11,12} agree well with experiment, while DFT predicts lower values. As a test of validity, the variation of cohesive energy with volume was calculated. Fig. 7 compares the energy *vs.* volume curves for cementite generated by the present MEAM potential with DFT and experimental curves. During volume variation of cementite, the ratios between a , b and c lattice parameters were held constant. As noted before, DFT overestimates the cohesive energy and underestimates the volume. Therefore, the DFT curve sits to the left of the experimental curve, and it is shifted vertically to the experimental cohesive energy at equilibrium volume to aid the comparison with the experimental curve. The experimental curve was generated by Murnaghan's equation of state^{30,31} with the experimental bulk modulus, volume, and cohesive energy.⁴⁰ The experimental single-crystal bulk modulus of cementite has not yet been determined; therefore, the polycrystalline bulk modulus of cementite was used to generate the experimental curve.

A. Single-crystal elastic properties

The elastic moduli of cementite were calculated and compared to DFT and the interatomic potentials by Ruda et al.¹¹ and Henriksson et al.¹² as presented in Table VII. We used both $\delta = 0.5\%$ and $\delta = 0.1\%$ that produced the same result. These results show that the present MEAM potential for Fe-C alloy predicts cementite to be stable (positive elastic constants) and their values are reasonably close to those predicted by DFT. How-

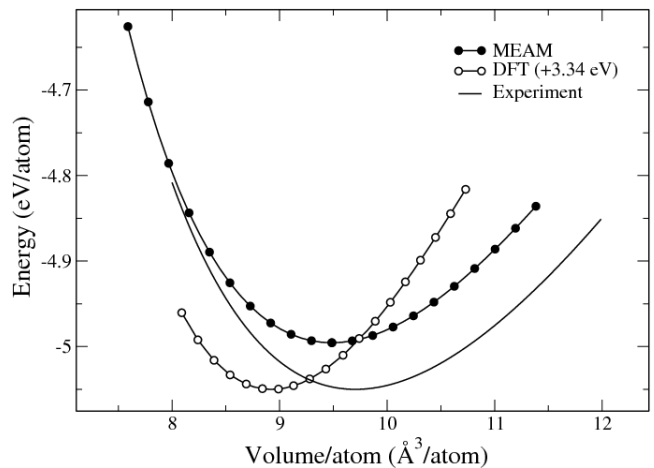


FIG. 7. Comparison of energy *vs.* volume curves for cementite. The solid curve is constructed from experimental values of the cohesive energy, polycrystalline bulk modulus, and equilibrium volume of cementite. For comparison, the DFT curve is shifted vertically to the experimental cohesive energy at the equilibrium volume.

TABLE VI. Material properties of cementite: the heat of formation ΔH_f (eV/atom); the equilibrium volume Ω_0 ($\text{\AA}^3/\text{atom}$); the lattice parameters a , b , and c (\AA). The predictions from the present work (MEAM) are compared with those from DFT and other interatomic potentials^{11,12}. Experimental values are given in parentheses.

Property	DFT (Expt.)	MEAM	Ruda	Henriksson
ΔH_f	0.01 (0.05 ^a)	0.06	0.18	0.03
Ω_0	8.49 (9.71 ^b)	9.49	9.11	9.33
a	4.91 (5.09 ^b)	5.05	5.14	5.09
b	6.63 (6.74 ^b)	6.69	6.52	6.52
c	4.38 (4.53 ^b)	4.49	4.35	4.50

^a Meschel et al.⁶

^b Umemoto et al.⁴¹

ever, the present MEAM—and other interatomic potentials in the literature—could not reproduce the low value of c_{44} reported by DFT.³⁹

TABLE VII. Single-crystal elastic moduli, C_{xy} (GPa) of cementite. The predictions from the present work (MEAM) are compared with those from DFT³⁹ and other interatomic potentials^{11,12}.

Property	DFT	MEAM	Ruda	Henriksson
c_{11}	395	303	263	363
c_{22}	347	216	219	406
c_{33}	325	307	247	388
c_{12}	158	126	176	181
c_{23}	163	110	143	130
c_{13}	169	157	146	166
c_{44}	18	249	77	91
c_{55}	134	236	95	125
c_{66}	135	227	123	134

B. Polycrystalline elastic properties

Theoretical upper and lower bounds for the polycrystalline bulk modulus (B) and shear modulus (G) were calculated using the single-crystal elastic constants according to methods by Reuss and Voigt.^{39,42} The true polycrystalline B and G were then estimated using Hill's average.^{39,43} Young's modulus (Y) and Poisson's ratio (ν) were calculated by using:³⁹

$$Y = 9BG/(3B + G) \quad (1)$$

$$\nu = (3B/2 - G)/(3B + G) \quad (2)$$

Polycrystalline elastic moduli predicted by our MEAM potential are presented in Table VIII, in comparison with DFT, experiment, and interatomic potentials by Ruda et al.¹¹ and Henriksson et al.¹² The elastic constants predicted by DFT are in excellent agreement with experiment. The present MEAM gives the best agreement with experiment among the three interatomic potentials for B ; however, the present MEAM prediction of ν is significantly lower than its experimental value. Ruda's potential predicts the best agreement with experiment for G and ν .

TABLE VIII. Polycrystalline cementite properties: bulk modulus B (GPa), shear modulus G (GPa), Young's modulus Y (GPa), and Poisson's ratio ν . The predictions from the present work (MEAM) are compared with those from DFT³⁹, and other interatomic potentials^{11,12}. Experimental values are given in parentheses.

Property	DFT (Expt.)	MEAM	Ruda	Henriksson
B	224 (175±4 ^a)	174	183	234
G	72 (74 ^b)	146	69	114
Y	194 (177 ^c , 196 ^d , 200 ^b)	343	184	293
ν	0.36 (0.36 ^b)	0.17	0.33	0.29

^a Scott et al.⁴⁴

^b Laszlo et al.⁴⁵

^c Mizubayashi et al.⁴⁶

^d Umemoto et al.⁴¹

C. Surface energies

Calculations were performed on (001), (010), and (100) surfaces to determine the surface formation energy. Table IX compares the surface formation energies of the present MEAM to DFT and the interatomic potential by Ruda et al.¹¹ The atoms near the surfaces are fully relaxed to allow reconstruction if necessary. The predicted surface energies have the same order of magnitude as DFT results. However, the present MEAM gives a wrong order of stability among the three surfaces.

TABLE IX. Surface energies (J/m^2) of cementite. The predictions from the present work (MEAM) are compared with those from DFT⁴⁷ and other interatomic potentials¹¹.

Surface	DFT	MEAM	Ruda
(001)	2.05	2.30	1.96
(010)	2.26	1.81	2.00
(100)	2.47	1.79	2.34

V. THERMAL PROPERTIES OF CEMENTITE

A. Thermal stability of cementite

The stability of cementite at high temperatures was investigated through molecular dynamics (MD) simulations in a canonical (NVT) ensemble at 300 K and 800 K. At the end of these MD simulations, cementite retained its crystalline structure, affirming its stability at high temperatures. The present Fe-C MEAM potential was also used to predict several thermal properties of cementite. In this section, we present calculations for predicting melting temperature and variation of specific heat and volume of cementite with respect to temperature.

B. Melting temperature simulation

The melting temperature of cementite is not well defined due to its instability at high temperatures. The Fe-C phase diagram indicates a eutectic point at 1420 K,⁷ where liquid consisting of Fe and C solidifies to form austenite and cementite crystals. For the purpose of this calculation, we considered the melting temperature of cementite to be the temperature when cementite loses its crystal structure and becomes a random collection of Fe and C atoms similar to the eutectic point. The melting temperature calculation can be done using a single-phase simulation box. However, the single phase method generally overestimates the melting temperature due to the lack of the interface effects.⁴⁸ To avoid this superheating problem and predict the melting temperature more accurately, we used a two-phase simulation box that contains both solid and liquid phases.

1. Preparation of two-phase simulation box

We performed two-phase simulations (TPS) in the isothermal-isobaric (NPT) ensemble to determine the melting temperature of cementite. The simulation box contained both solid and liquid phases of cementite. First a supercell containing $14 \times 7 \times 7$ unit cells of cementite (10976 atoms) was heated via MD runs in the NPT ensemble with $T = 1200$ K and $P = 0$. Next, one half of the atoms in the supercell were fixed in their positions and MD runs were carried out for the other half in the

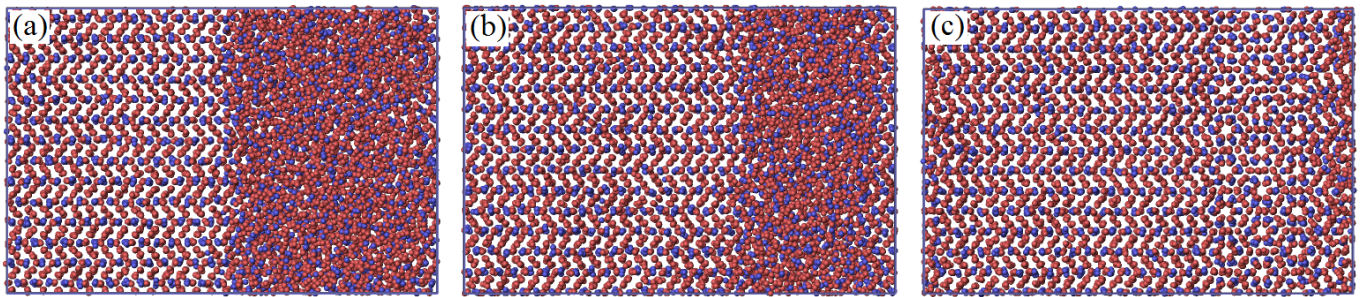


FIG. 8. (Color online) Snapshots of the two-phase MD simulation in the NPT ensemble with $T = 1420$ K and $P = 0$. Red spheres are Fe atoms and blue spheres are C atoms. (a) Initial state of the simulation box, which contains both liquid and solid phases of cementite. (b) Intermediate state of the simulation box at 16 ns, as the solid phase propagates to the liquid phase. (c) Final state of the simulation box at 32 ns, when the entire system has turned into the solid phase.

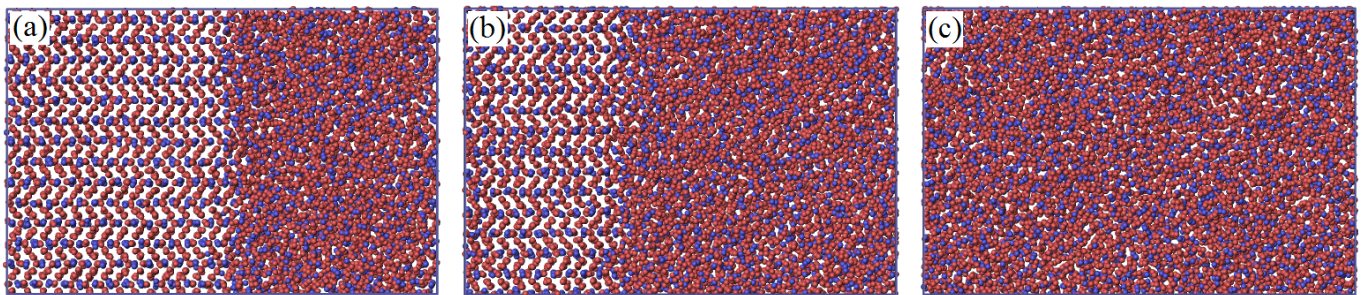


FIG. 9. (Color online) Snapshots of the two-phase MD simulation in the NPT ensemble with $T = 1430$ K and $P = 0$. Red spheres are Fe atoms and blue spheres are C atoms. (a) Initial state of the simulation box, which contains both liquid and solid phases of cementite. (b) Intermediate state of the simulation box at 20 ns, as the liquid phase propagates to the solid phase. (c) Final state of the simulation box at 30 ns, when the entire system has turned into the liquid phase.

NPT ensemble with a sufficiently high temperature (such as $T = 4000$ K) and $P = 0$ to create a liquid phase. The resulting supercell was then subjected to MD runs in the NPT ensemble with $T = 1500$ K (close to $T = 1200$ K but still higher than the expected melting temperature) and $P = 0$, still keeping the same half of the atoms fixed. The result of this process was a supercell containing solid cementite at 1200 K in one half, and liquid cementite at 1500 K in the other. This ensures a minimum difference of stress between atoms in liquid and solid phases of the supercell. This supercell was then used in the simulations of solidification and melting of cementite.

2. Two-phase simulation

The two-phase supercell prepared in the previous section was heated by MD runs in the NPT ensemble where the temperature T was increased from 1000 K to 1600 K in 100 K intervals. Each system ran for 1.6 ns of simulation time. The phase change of the two-phase simulation box was visually monitored. At 1400 K, the solid phase of the simulation box progressed to occupy the entire box, and at 1500 K the liquid phase of the simulation box progressed to occupy the entire box. Next, the initial two-phase simulation box was heated from 1400 K to

1500 K in 10 K intervals using NPT MD runs. Each system was equilibrated for at least 5×10^6 time steps, where each time step was 2 fs, totaling to 10 ns. The final state of the system was visually inspected. If the final state appeared to have both liquid and solid phases, more MD runs were performed until the final state of the supercell contained only one phase. Some systems required as much as 32 ns of MD runs to arrive at a single phase. The transformation of the two-phase simulation box to a one-phase simulation box near the predicted melting temperature is presented in Fig. 8 and Fig. 9. The total energy, volume, and pressure of the systems were determined through averaging the values of the final 40,000 time steps (80 ps) of each simulation.

In Fig. 10 we plot the total energy, volume, specific heat, and the derivative of volume as functions of temperature. Experimental data for specific heat and volume are not available for the 1400-1500 K temperature range. Available experimental data are the heat capacity of $3.6 k_B/\text{atom}$ at 1023 K,⁴⁹ which converts to 3.4 eV/K for the current simulation, and the experimental volume of $10 \text{ \AA}^3/\text{atom}$ at 1070 K.⁵⁰ Specific heat and volume determined by Dick et al. from the first-principles calculations⁵¹ done on the solid phase of cementite are included for comparison in Figs. 10(b) and (c). Since Dick and coworkers used a single-phase simulation box,

their simulation clearly shows superheating causing the melting temperature to be overestimated. This can be attributed to the absence of the solid-liquid interface in single phase simulations. In Fig. 10(c) the specific heat shows a peak between 1420 K and 1430 K. Therefore we assign 1425 ± 5 K as the melting temperature of cementite. This is in good agreement with the experimental eutectic point of 1420 K.⁷

VI. SUMMARY AND CONCLUSION

We investigated the properties of cementite using an interatomic potential developed within the MEAM formalism. Previously developed single element interatomic potentials for Fe and C were used to develop the Fe-C alloy MEAM potential. The single element potential for C predicts graphite and diamond as minimum energy structures with almost degenerate energies. MEAM potentials for pure elements predict the heat of formation, bulk moduli, and lattice constants of Fe and C in their natural crystal structures in good agreement with experimental data. The alloy potential for the Fe-C system was developed to reproduce heat of formation of Fe-C alloys in B₁, L₁₂, and cementite crystal structures, as well as the interstitial energies of C in bcc Fe. The Fe-C potential was validated by investigating the energy variation with respect to volume of Fe-C alloys in B₁ and L₁₂ structures. The validated potential was used to predict structural, elastic,

and thermal properties of cementite. Structural properties tested included the heat of formation, the equilibrium lattice constants, the equilibrium volume, and the energy variation with respect to volume. MEAM predictions are in good agreement with DFT and experiment. The nine single crystal elastic constants were calculated and used to estimate polycrystalline bulk modulus, shear modulus, Young's modulus, and Poisson's ratio of cementite. Surface energies for (001), (010), and (100) surfaces were also calculated and compared. Melting temperature and the variation of specific heat and volume with respect to temperature were predicted by two-phase (solid/liquid) MD simulations. The present MEAM potential predicted the melting temperature of cementite to be 1425 ± 5 K, which is in good agreement with the eutectic point of 1420 K given in the Fe-C phase diagram.

VII. ACKNOWLEDGMENTS

We are grateful to A.B. Belonoshko for his suggestions in conducting the two-phase melting simulations. This work was supported in part by the Department of Energy, grants DE-EE0002323 and DE-FC26-06NT2755. Computer time allocation has been provided by the High Performance Computing Collaboratory (HPC²) at Mississippi State University.

* Author to whom correspondence should be addressed; kimgsg@hpc.msstate.edu

¹ M. I. Baskes, Phys. Rev. B **46**, 2727 (1992).

² M. S. Daw and M. I. Baskes, Phys. Rev. B **29**, 6443 (1984).

³ B.-J. Lee, M. Baskes, H. Kim, and Y. Koo Cho, Phys. Rev. B **64**, 184102 (2001).

⁴ B. Lee, Acta Materialia **54**, 701 (2006).

⁵ C. F. Fang, M. A. v. Huis, B. J. Thijssen, and H. W. Zandbergen, Phys. Rev. B (2012).

⁶ S. Meschel and O. Kleppa, Journal of Alloys and Compounds **257**, 227 (1997).

⁷ W. Callister and D. Rethwisch, *Materials science and engineering: an introduction*, 7th ed. (Wiley New York, 2007) pp. 290–293.

⁸ C. Becquart, J. Raulot, G. Bencteux, C. Domain, M. Perez, S. Garruchet, and H. Nguyen, Computational Materials Science **40**, 119 (2007).

⁹ T. T. Lau, C. J. Först, X. Lin, J. D. Gale, S. Yip, and K. J. V. Vliet, Phys. Rev. Lett. **98**, 215501 (2007).

¹⁰ D. J. Hepburn and G. J. Ackland, Phys. Rev. B **78**, 165115 (2008).

¹¹ M. Ruda, D. Farkas, and G. Garcia, Computational Materials Science **45**, 550 (2009).

¹² K. Henriksson and K. Nordlund, Physical Review B **79**, 1 (2009).

¹³ A. Duff and M. Sluiter, Materials Transactions **51**, 675 (2010).

¹⁴ P. Erhart, N. Juslin, O. Goy, K. Nordlund, R. Mller, and K. Albe, Journal of Physics: Condensed Matter **18**, 6585 (2006).

¹⁵ K. Albe, K. Nordlund, and R. S. Averback, Phys. Rev. B **65**, 195124 (2002).

¹⁶ T. Lee, M. I. Baskes, S. M. Valone, and J. D. Doll, Los Alamos Preprint:LA-UR 11-03286 (2011).

¹⁷ J. Uddin, M. I. Baskes, S. G. Srinivasan, T. R. Cundari, and A. K. Wilson, Phys. Rev. B **81**, 104103 (2010).

¹⁸ Steve and Plimpton, Journal of Computational Physics **117**, 1 (1995).

¹⁹ S. Plimpton *et al.*, “Lammps-large-scale atomic/molecular massively parallel simulator,” April 2011 version.

²⁰ G. Kresse and J. Hafner, Phys. Rev. B **47**, 558 (1993).

²¹ G. Kresse and J. Furthmüller, Phys. Rev. B **54**, 11169 (1996).

²² G. Kresse and D. Joubert, Phys. Rev. B **59**, 1758 (1999).

²³ J. P. Perdew, K. Burke, and M. Ernzerhof, Phys. Rev. Lett. **77**, 3865 (1996).

²⁴ H. Monkhorst and J. Pack, Phys. Rev. B **13**, 5188 (1976).

²⁵ M. Methfessel and A. T. Paxton, Phys. Rev. B **40**, 3616 (1989).

²⁶ M. Tschoopp, K. Solanki, M. Baskes, F. Gao, X. Sun, and M. Horstemeyer, Journal of Nuclear Materials, (2011).

²⁷ M. McKay, R. Beckman, and W. Conover, Technometrics **42**, 55 (2000).

²⁸ P. H. T. Philipsen and E. J. Baerends, Phys. Rev. B **54**, 5326 (1996).

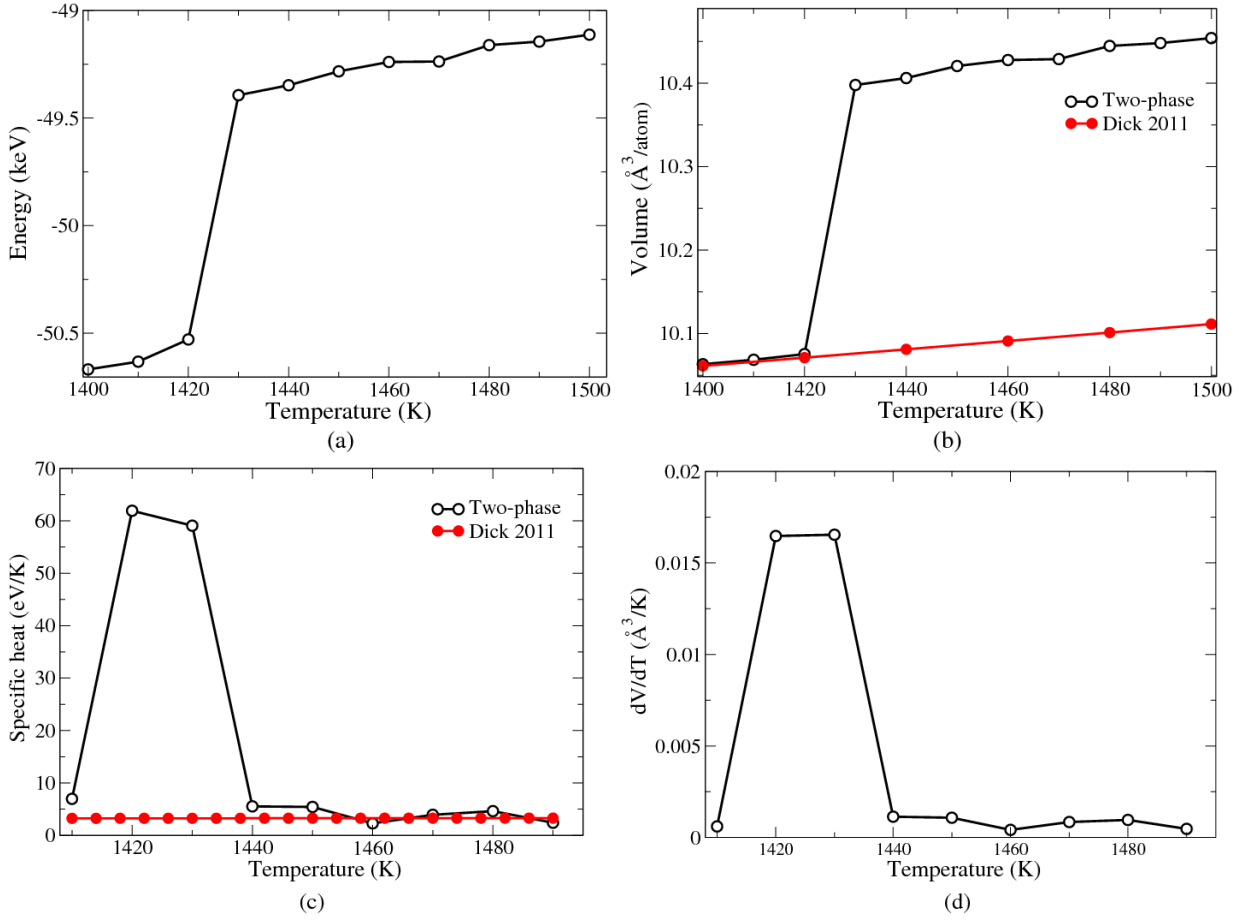


FIG. 10. Variation of properties of the two-phase system over the temperature. (a) Total energy of the system. (b) (Color online) Volume of the system. Red curve is first-principles data by Dick et al.⁵¹ (c) (Color online) Specific heat of the system. Red curve is the first-principles data. (d) dV/dT of the system.

- ²⁹ A. Devey and N. H. de Leeuw, Phys. Rev. B **82**, 235112 (2010).
- ³⁰ F. D. Murnaghan, Proceedings of the National Academy of Science **30**, 244 (1944).
- ³¹ F. Murnaghan, *Finite deformation of an elastic solid* (Dover New York, 1967).
- ³² J. H. Rose, J. R. Smith, F. Guinea, and J. Ferrante, Phys. Rev. B **29**, 2963 (1984).
- ³³ M. T. Yin and M. L. Cohen, Phys. Rev. B **29**, 6996 (1984).
- ³⁴ C. S. Wang, B. M. Klein, and H. Krakauer, Phys. Rev. Lett. **54**, 1852 (1985).
- ³⁵ J. Donohue, *The structures of the elements* (R.E. Krieger Pub. Co., Malabar, Fla., 1982) p. 256.
- ³⁶ H. J. McSkimin, J. P. Andreatch, and P. Glynn, Journal of Applied Physics **43**, 985 (1972).
- ³⁷ S. Fahy and S. G. Louie, Phys. Rev. B **36**, 3373 (1987).
- ³⁸ O. L. and Anderson, Journal of Physics and Chemistry of Solids **27**, 547 (1966).
- ³⁹ C. Jiang, S. G. Srinivasan, a. Caro, and S. a. Maloy, Journal of Applied Physics **103**, 043502 (2008).
- ⁴⁰ J. Häglund, G. Grimvall, and T. Jarlborg, Phys. Rev. B **44**, 2914 (1991).
- ⁴¹ M. Umemoto, Z. Liu, K. Masuyama, and K. Tsuchiya, Scripta Materialia **45**, 391 (2001).
- ⁴² K. Panda and K. R. Chandran, Acta Materialia **54**, 1641 (2006).
- ⁴³ R. Hill, Proceedings of the Physical Society. Section A **65**, 349 (1952).
- ⁴⁴ H. P. Scott, Q. Williams, and E. Knittle, Geophys. Res. Lett. **28**, 1875 (2001).
- ⁴⁵ F. Laszlo and H. Nolle, Journal of the Mechanics and Physics of Solids **7**, 193 (1959).
- ⁴⁶ H. Mizubayashi, S. Li, H. Yumoto, and M. Shimotomai, Scripta Materialia **40**, 773 (1999).
- ⁴⁷ W. Chiou, Surface Science **530**, 87 (2003).
- ⁴⁸ A. B. Belonoshko, Geochimica et Cosmochimica Acta **58**, 4039 (1994).
- ⁴⁹ G. Naeser, Mitt. Kais.-Wilh.-Inst. Eisenforsch **16**, 207 (1934), as reported in Dick et al.⁵¹.
- ⁵⁰ R. C. Reed and J. H. Root, Scripta Materialia **38**, 95 (1997), as reported by Dick et al.⁵¹.
- ⁵¹ A. Dick, F. Körmann, T. Hickel, and J. Neugebauer, Phys. Rev. B **84**, 125101 (2011).